nature communications

Article

https://doi.org/10.1038/s41467-025-59258-4

Duality and degeneracy lifting in two-dimensional electron liquids on $SrTiO_3(001)$

Received: 8 August 2024

Accepted: 11 April 2025

Published online: 17 May 2025

Check for updates

Igor Sokolović[1] ✉, Eduardo B. Guedes[2], Thomas P. van Waas[3], Fei Guo[4], Samuel Poncé[3,5], Craig Polley[6], Michael Schmid[1], Ulrike Diebold[1], Milan Radović[2], Martin Setvín[1,7] & J. Hugo Dil[2,4] ✉

Two-dimensional electron liquids (2DELs) have increasing technological relevance for ultrafast electronics and spintronics, yet significant gaps in their fundamental understanding are exemplified on the prototypical $SrTiO_3$. We correlate the exact $SrTiO_3(001)$ surface structure with distinct 2DELs through combined microscopic angle-resolved photoemission spectroscopy and noncontact atomic force microscopy on truly bulk-terminated surfaces that alleviate structural uncertainties inherent to this long-studied system. The SrO termination is shown to develop a 2DEL following the creation of oxygen vacancies, unlike the intrinsically metallic TiO_2 termination. Differences in degeneracy of the 2DELs, with nearly the same band filling and identical band bending, are assigned to polar distortions of the Ti atoms in combination with spin order, supported with the extraction of fundamental electron-phonon coupling strength. These results not only resolve the ambiguities regarding 2DELs on $SrTiO_3$ thus far, but also pave the way to manipulating band filling and spin order in oxide 2DELs in general.

The extensive pursuit for the next-generation electronics steers towards low-dimensional systems. Here, $SrTiO_3$ – a model cubic perovskite oxide – plays a versatile role. Starting as a promising candidate for high-temperature superconductivity[1], through its potential as a gate dielectric with ϵ_r in the order of 10^3 [2], and finally as an insulator that hosts highly mobile two-dimensional electron liquids (2DELs) at its bare surface[3–10] or when interfaced with other insulators[11–13]. Since the discovery of a 2DEL at the $LaAlO_3/SrTiO_3$ interface[14] it was the subject of two decades of research[15], but the concepts crucial for oxide electronics[16] such as the origin, creation, filling, and lifting of the spin degeneracy in these 2DELs remain debated. We directly elucidate and disentangle these fundamental phenomena by studying $SrTiO_3$ surfaces of unprecedented quality in direct and reciprocal space.

Most ambiguities related to the 2DELs on $SrTiO_3(001)$ stem from its elusive surface structure. They are commonly assumed as bulk-truncated, yet without real-space confirmation. Moreover, the tripartite bulk composition is sensitive to stoichiometry changes and the assumption of pristine surfaces is hardly warranted. Such ambiguities of the surface structure lead to inconclusive and commonly contradictory reports on the traits of 2DELs on $SrTiO_3(001)$.

In this work, we reveal the sensitivity of the 2DELs towards the exact surface termination, and directly observe the underlying mechanisms that define their properties.

Results and Discussion

Bulk-truncated $SrTiO_3(001)$ surface

With our recently developed cleaving technique that exploits the strain-induced ferroelectric phase transition in $SrTiO_3$[17], we routinely create surfaces that are truly bulk-terminated, atomically flat, and well-defined at the atomic level as confirmed by noncontact atomic force

[1]Institute of Applied Physics, TU Wien, Vienna, Austria. [2]Center for Photon Science, Paul Scherrer Institut, Villigen, Switzerland. [3]European Theoretical Spectroscopy Facility, Institute of Condensed Matter and Nanosciences, Université catholique de Louvain, Louvain-la-Neuve, Belgium. [4]Institut de Physique, École Polytechnique Fédérale de Lausanne, Lausanne, Switzerland. [5]WEL Research Institute, Wavre, Belgium. [6]MAX IV Laboratory, Lund University, Lund, Sweden. [7]Department of Surface and Plasma Science, Faculty of Mathematics and Physics, Charles University, Prague, Czech Republic.
✉e-mail: igor.sokolovic@tuwien.ac.at; hugo.dil@epfl.ch

https://doi.org/10.1038/s41467-025-59258-4

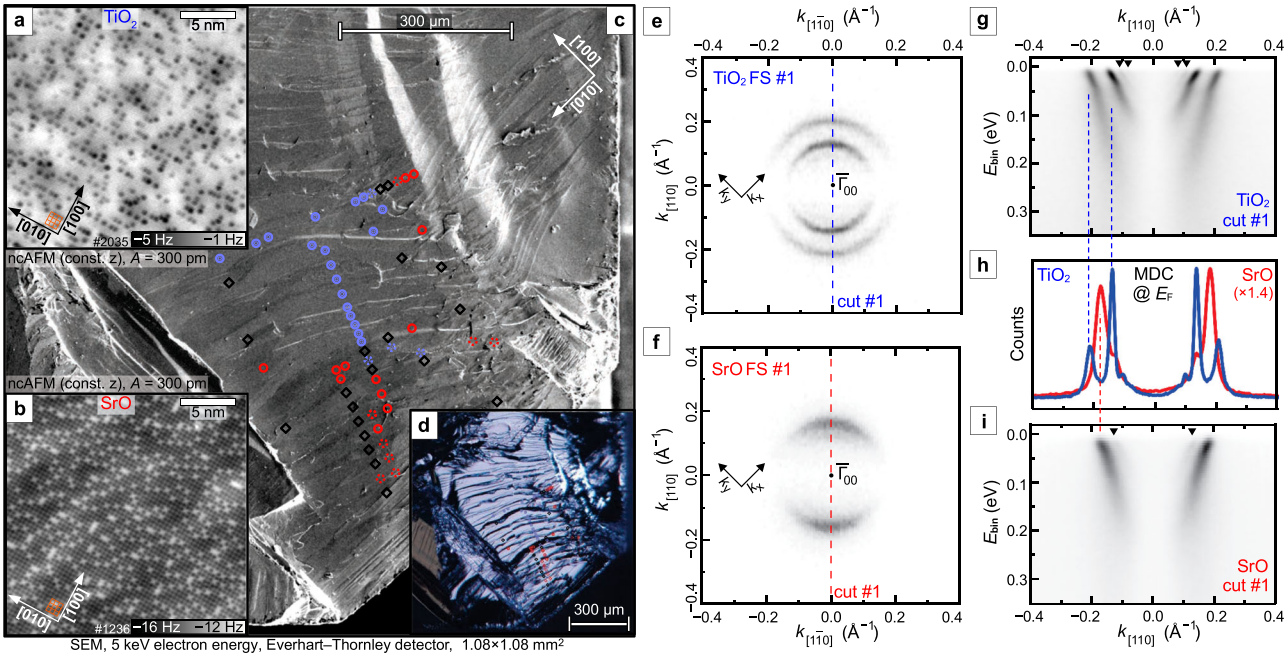

Fig. 1 | Two distinct 2DELs on a truly bulk-terminated $SrTiO_3$(001)-(1 × 1) surface. Atomically resolved ncAFM images obtained on the (**a**) TiO_2 termination with 14% of Sr adatoms and (**b**) SrO termination with 14% of Sr vacancies. The point defects are intrinsic to a $SrTiO_3$(001) surface cleaved via the strain-induced ferroelectric phase transition. An orange grid indicates the surface unit cells. The counterpiece of the cleaved $SrTiO_3$(001) surface investigated with ARPES displayed in a (**c**) secondary-electron SEM image and in an (**d**) optical photograph: Dark SEM contrast corresponds to TiO_2- and light gray to SrO-terminated surface regions. Blue markers in (**c**, **d**) indicate where the measured Fermi surface shows a double ring (**e**), while red markers show regions with a single ring (**f**), obtained with $h\nu$=47 eV (FS #1). SEM was performed on a counter-piece of the ARPES-investigated surface, so the contrast is inverted. Black diamonds and broken colored circles are positioned where ARPES detected an ill-defined Fermi surface or a Fermi surface that only weakly resembles one of the two well-defined ones, respectively (shown in Supplementary Note 4). Marker sizes are to scale with the 10 μm radius of the beam spot. The corresponding band dispersion maps along the $k_{[110]}$ direction (dashed lines, cut #1) are shown in (**g**, **i**). MDCs along the dashed lines in (**e**, **f**) at E_F are shown in (**h**). The triangular markers in (**g**, **i**) indicate the quantum-well replicas of the main bands, visible as faint inner bands.

microscopy (ncAFM). This is in sharp contrast to differently-prepared surfaces that are either contaminated, reconstructed, or disordered, due to the thermal instability of the (1 × 1)-terminated $SrTiO_3$(001) surface[18].

Figure 1 shows ncAFM, angle-resolved photoemission spectroscopy (ARPES), and scanning electron microscopy (SEM) data on a truly bulk-terminated $SrTiO_3$(001) surface. Our cleaving procedure always produces surfaces with both terminations (TiO_2 and SrO), each covered with the same concentration of complementary point defects: TiO_2 with 14% of Sr adatoms (Sr_{ad}) and SrO with 14% of strontium vacancies (V_{Sr}), resolved by ncAFM in Fig. 1a, b, respectively. Their presence is unavoidable as they compensate the polarity induced during successful cleaving[17,19,20], but, in turn, guarantee the structure of our well-cleaved surface areas. The O-terminated ncAFM tip[21] detects Sr_{ad} as dark spheres (attraction) and V_{Sr} as bright "x"-shaped features (absence of attractive signal).

At the standard doping level of 0.5 weight percent (wt%) of Nb, the domains of these two surface terminations are sufficiently large to be individually studied by synchrotron-based ARPES with a beam spot diameter of ≈10 μm. On a mesoscopic scale, the two terminations can be distinguished by SEM even after transfer through air: TiO_2- and SrO-terminated surface regions are imaged as dark and bright, respectively (details in the Supplementary Information (SI); Supplementary Note 1). Figure 1c shows a SEM micrograph of the counterpiece (i.e. the other side after cleavage) of the surface studied under synchrotron light; an optical photograph is shown in Fig. 1d. The counterpiece of the cleavage has the same geometry but the opposite distribution of surface terminations[22] (more details in Supplementary Note 1), that are recognized as the opposite SEM contrast. The lateral positions of the ARPES measurements are superimposed on this SEM image, indicating that on the surface where ARPES was performed, a split and a degenerate 2DEL appears on the TiO_2 and SrO termination, respectively. Symmetry between the main and the counter-piece of cleaved $SrTiO_3$(001) surfaces has been verified for around 100 cleaves over the years[22]. With SEM acting as a bridge between synchrotron and ncAFM measurements, we proceed to correlate the 2DEL properties with the surface structure.

Termination-specific 2DELs

The two terminations formally differ in one atomic layer and host almost identical 2DELs, making it hard to discriminate between the two using X-ray photoelectron spectroscopy (Supplementary Note 7), in contrast to some other systems[23] where the chemical and electronic environment is significantly different for the two terminations. However, each displays a distinct Fermi surface (FS) as witnessed by ARPES (photon energy $h\nu$=47 eV) in Fig. 1e, f. Both are derived from Ti $3d_{xy}$ orbitals[3], but the TiO_2 termination is characterized by two sharp rings, while the SrO termination is characterized by a single ring. The purity of the cleaved surfaces and the resulting high quality of the ARPES data allow us to detect additional faint bands visible at smaller binding energies (black triangles in Fig. 1g and i) on both the TiO_2 and the SrO termination: two faint bands with smaller splitting on the former, and a single faint band at the latter. These states are assigned to the next N=2 quantum-well replicas[24]. Spectra acquired at different spots on the sample demonstrate that the presented data is representative of the TiO_2 and SrO terminations throughout the sample, as demonstrated in Supplementary Note 2 where several raw spectra are displayed. It is noteworthy that the spectra presented in Figs. 1 and 2 is of exceptional quality; in most spectra obtained by us the N=2 quantum-well replicas are not discernable on either surface termination (Supplementary

https://doi.org/10.1038/s41467-025-59258-4

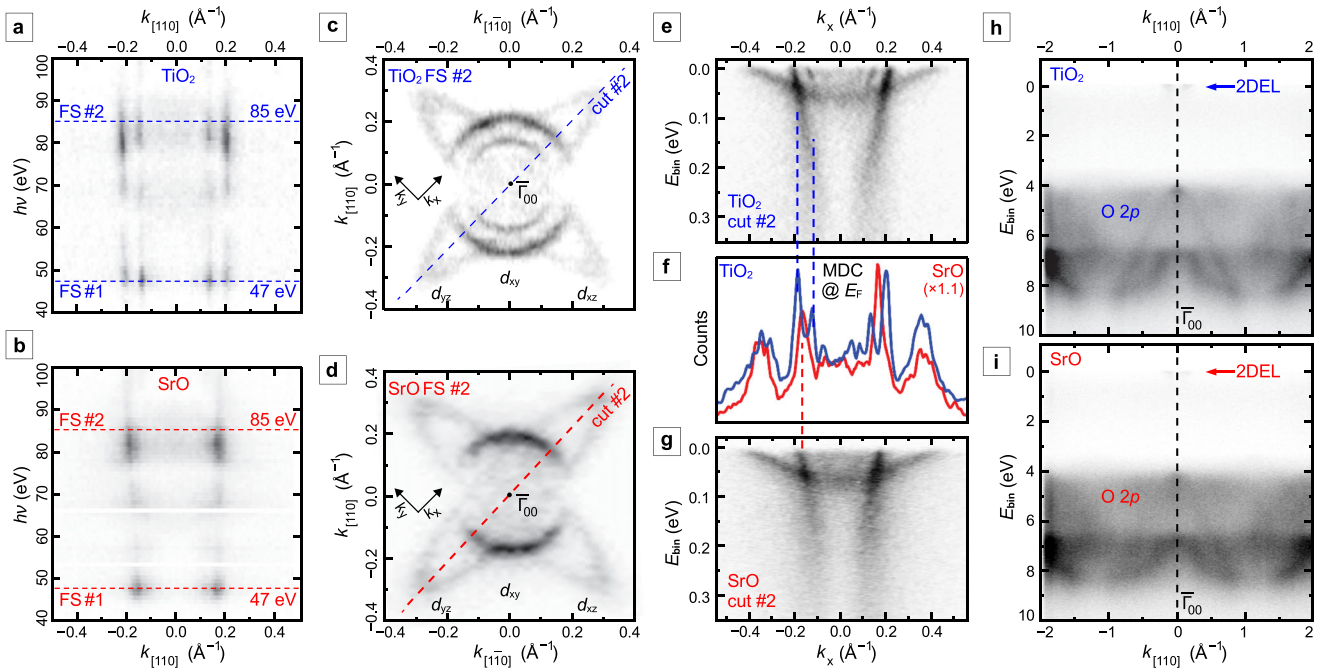

Fig. 2 | Details of the 2DELs on TiO_2- and SrO-terminated surfaces. Photon-energy dependence of the 2DEL formed on the (**a**) TiO_2- and (**b**) SrO-terminated surfaces. The Fermi surface maps measured with $h\nu$=85 eV (FS #2) are shown in (**c**, **d**), and the corresponding band dispersion maps along the k_x direction (cut #2) in (**e**, **g**), with a comparison of the MDCs at the Fermi level displayed in (**f**). **h**, **i** O 2*p* band of the TiO_2 and SrO-terminated surface, respectively, measured with $h\nu$=170 eV.

Notes 2 and 3). In contrast, conchoidal surface regions, which lack a well-defined atomic structure[17], exhibit a variety of less-defined FSs that often resemble a combination of the well-defined FSs obtained on the two terminations (Supplementary Note 4). The assignment of the two distinct 2DELs to two distinct surface terminations is further supported by real-space ncAFM experiments below (Fig. 3).

Band maps measured along the $k_{[110]}$ direction (Fig. 1g, i) show that these states at the two terminations have a similar dispersion, while the main difference lies in the splitting of the bands. A comparison of the momentum distribution curves (MDCs) at the Fermi level E_F in Fig. 1h highlights some important differences between the TiO_2- and SrO-terminated surfaces. The lines on the former are significantly sharper and the peak maximum of the latter lies between the split bands of the former. This difference cannot be explained by a spectral broadening of the two sharp bands on the TiO_2 termination, making them appear as one band on the SrO side (Supplementary Note 5). The difference in band splitting between the pure TiO_2- and SrO-terminated areas can be clearly observed experimentally when the ARPES spectra is collected from a surface area that contains a smooth transition between the two (Supplementary Note 6). Furthermore, the intensity obtained for the SrO termination (Fig. 1h) needs to be multiplied by a factor 1.4 to be comparable to the TiO_2 termination. Considering the limited mean free path of the photoelectrons, this lower intensity on the SrO termination agrees with the localisation of the 2DEL in the subsurface TiO_2 plane.

Figure 2 presents more details of the electronic structure of the 2DELs at both terminations, with the extracted experimental values of k_F, carrier densities n_{2D}, and band bottoms E_{bot} laid out in Supplementary Table 1. The observed band filling, as extracted from k_F, is larger than those where the formation of polaronic replicas in the ARPES data can be expected[25,26]. The absence of dispersion in the photon energy scans (Fig. 2a, b) confirm that the d_{xy}-derived states on both terminations are two-dimensional. Additionally, the resonant enhancements on both terminations occur in the same energy ranges, again indicating their similar orbital composition.

At $h\nu$=85 eV, in addition to Ti 3d_{xy} states of Fig. 1e–i, the Ti 3d_{xz}- and d_{yz}-derived states[3] are visible in the FS maps (Fig. 2c, d). The Fermi wavevectors k_F and band bottoms of these "heavy" bands (Fig. 2e–g) are – within the experimental resolution – the same for both terminations (Supplementary Table 1). The quality of the in-situ cleaved $SrTiO_3$(001) surface allows us to clearly record the O 2*p* band on both terminations (Fig. 2h, i). These measurements were performed with $h\nu$=170 eV, allowing the observation of the full first Brillouin zone in the ⟨110⟩ direction. The similar data quality on both terminations reiterates that the differences between the two terminations recorded with ARPES are intrinsic and unrelated to surface quality. In contrast, ARPES collected on ill-defined surface regions (conchoidal) and regions with macroscopic defects (Supplementary Note 4) exhibit a significant reduction in data quality.

Origin of the 2DELs

A 2DEL is known to appear at $SrTiO_3$(001) surfaces after prolonged synchrotron irradiation[3,4,7,27–29], hinting towards defect-induced population. Both distinct 2DELs on our cleaved $SrTiO_3$(001) surfaces develop much faster: The FS on TiO_2 termination becomes clear and intense in a $\lesssim$2 s time frame (at around $5 \times 10^{10} h\nu/\mu m^2$), whereas the FS at the SrO termination develops more slowly, and becomes well-defined only after ≈30 s (Supplementary Movies 1 and 2). This indicates fundamental differences between the two terminations, but also highlights how very little defects are necessary for their creation on the TiO_2 and SrO terminations. In comparison, conchoidal surface regions that lack proper atomic order and intrinsic polarization exhibited slowly developing, badly defined FSs (Supplementary Note 4).

In our scanning tunneling spectroscopy (STS) experiments (Fig. 3d) the TiO_2 termination is observed to be metallic immediately after cleaving[17]. Positive Sr_{ad} ions compensate the strain-induced polarity during cleaving, yet their presence induces downward band bending on the extrinsically n-doped crystals. The presence of distinct in-gap filled states in STS on the TiO_2 termination is consistent with the ARPES measurements, but the tip-induced shifting of all energy states

https://doi.org/10.1038/s41467-025-59258-4

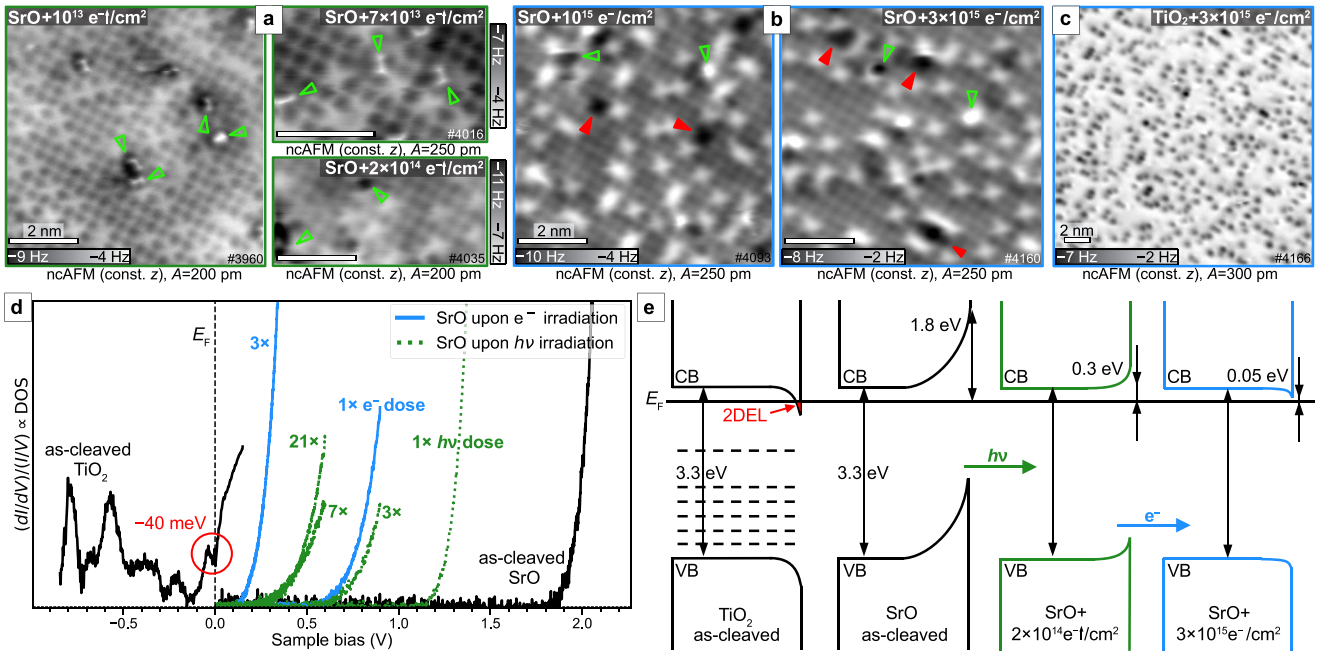

Fig. 3 | 2DEL formation mechanism on the SrO-terminated surface emulated with the irradiation of laboratory Al *Kα* X-rays and 47 eV electrons. Atomically resolved ncAFM images obtained on (**a**) the SrO termination irradiated with several doses of X-rays (measured as photocurrent "$e^-\uparrow$"; 1× *hν* dose equals $10^{13} e^-\uparrow/cm^2$), (**b**) SrO termination and (**c**) TiO_2 termination after two different doses of electron irradiation (1× e^- dose equals $10^{15} e^-/cm^2$). Green hollow arrows indicate features attributed to adsorbates and red filled arrows indicate oxygen vacancies that appear exclusively on the SrO termination after irradiation with 47 eV electrons. 2 nm scale bar in all ncAFM panels. **d** STS shows the effect of the irradiation on the density of states: metallic TiO_2 with a distinct DOS feature just below the Fermi level (−40 meV) is unaffected, while photoemission and the formation of oxygen vacancies bring the onset of the SrO conduction band closer to the Fermi level following progressive X-ray and electron irradiation. **e** Illustration of the conduction band (CB), valence band (VB), Fermi level (full line E_F), and in-gap states (broken lines on TiO_2) of the two terminations upon irradiation: TiO_2 remains metallic with an intrinsic 2DEL, while the upward band bending on SrO is reduced through photoemission followed by the additional downward band bending induced by the formation of oxygen vacancies.

in STS and the different tunneling probabilities to distinct $d_{xz/yz}$ and d_{xy} derived states thwart the direct comparison between the two techniques.

Ab-initio slab calculations show that for the TiO_2 termination the d_{xy} states are above the heavy bands in energy[3,8], not at higher binding energy as seen in the ARPES data. This suggests the possibility that the $\lesssim$2 s delay in detection of a 2DEL on TiO_2 is due to the fact that the d_{xy} bands become populated by photo-excited, and incoherently scattered, secondary electrons following a small amount of synchrotron irradiation. Alternatively, a small amount of adsorbates that trap the charges are quickly removed by the synchrotron light via dissociation/association and desorption[21]. In either scenario, the creation of defects under synchrotron irradiation is clearly not necessary for a TiO_2 termination to host a fully developed 2DEL.

The SrO termination is wide-gap semiconducting immediately upon cleaving[17], promoted by the negative V_{Sr}s that cause an upward band bending (Fig. 3d). The formation mechanism of a 2DEL, i.e., the semiconductor-to-metal transition on SrO, was investigated separately by progressive irradiation with in-house X-ray and electron sources at T=100 K, summarized in Fig. 3. Photoemission by Al *Kα* X-rays (measured as photo-current "$e^-\uparrow$") significantly reduces the upward band bending and brings the conduction band onset down by 1.5 eV towards the Fermi level due to the surface photovoltaic effect[30]. This downshift saturates with increasing X-ray dose (Fig. 3d) and, according to STS, is not enough to turn SrO metallic. Ionic defects were not observed with ncAFM following X-ray irradiation, except for the appearance of adsorbates (green hollow arrows in Fig. 3a), which can most likely be attributed to the contamination from the residual gas during X-ray irradiation of a sample held at 100 K. The formation of a 2DEL requires additional downward band bending. Without a synchrotron source, this was achieved by irradiation of the SrO termination with electrons of sufficient energy to create positively charged oxygen vacancies (V_Os) via the Knotek-Feibelman mechanism[31,32]. The V_Os were observed in ncAFM as dark defects in the O sublattice[33] only after 47 eV electron irradiation, marked by red filled arrows in Fig. 3b. A total of 0.05 monolayers coverage of V_Os was sufficient to bring the onset of the conduction band within 50 meV of the Fermi level according to STS (Fig. 3d). Taking into account tip-induced band bending, this will either be enough or a slightly higher concentration is expected to populate the conduction band. Therefore, in the 30 s of 47 eV synchrotron irradiation, a joint effect of reducing the band bending by photoemission and causing additional downward band bending by the creation of V_Os gradually develops a stable 2DEL on the SrO-terminated surface.

The electronic structure of a metallic TiO_2 termination remained unaffected under the same irradiation conditions, and no ionic defects were observed in ncAFM even after the highest dose of 47 eV electrons (Fig. 3c). In fact, the TiO_2 termination with Sr_{ad}s is more prone to adsorption of oxygen to neutralize the Sr ions[18] than the formation of V_Os. Therefore, we can safely exclude the relevance of oxygen vacancies for the formation of a 2DEL on the TiO_2-terminated surface, while their presence is necessary for a 2DEL on the SrO termination. In contrast to the pristine TiO_2 termination with scattered Sr_{ad}s, the presence of two types of oppositely charged defects (V_{Sr} and V_O) on the irradiated SrO termination can be expected to lead to larger fluctuations of the electrostatic potential and directly influence the wave function of the 2DEL below through electrostatic Gaussian disorder[34], thus explaining the larger linewidth and the observed multiple contributions, in contrast to the pristine TiO_2 termination.

In layer-by-layer MBE growth of $SrTiO_3$ films on a $SrTiO_3$ substrate, it is possible to control the preferential surface termination and it was found that the 2DEL develops more rapidly on the SrO-terminated

surface[9]. Unfortunately, that study gave no insight in the exact atomic structure at the surface and direct comparison with our results is thus impossible. It should be noted that the general development of the 2DEL was much slower than reported here, with a significantly lower band filling. In that context the 2DEL found on MBE-[9] and PLD-grown[7] films resemble each other with the added advantage of controlling the surface termination in the former. This highlights the importance to start from well-defined surfaces and the role played by the exact atomic structure on the 2DEL formation and properties.

Population

The nearly identical charge density of the 2DEL on both surface terminations as observed in ARPES (Supplementary Table 1), indicates a limit of the 2DEL carrier density at $SrTiO_3$(001) determined by the dielectric response of the material to the presence of a metallic surface, through a mechanism similar to Fermi level pinning at a metal-semiconductor interface. The observed similarities in the carrier densities on the two terminations (Supplementary Table 1) cannot be rationalized by electron donation from the the intrinsic or irradiation-induced defects on the TiO_2 and SrO termination, respectively: Real space measurements (Fig. 3) show that the concentration of these defects differs by an order of magnitude. Instead, the highly mobile 2DEL electrons stem from the bulk of the sample once the downward band-bending makes the Ti $3d_{xy}$ states energetically available. The V_Os on the SrO termination (and Sr_{ad}s on the TiO_2 termination) hence serve primarily as a band-bending-reversal mechanism, demonstrating a pathway to populating 2DELs with a small amount (≈1%) of external defects and thus maintaining relatively low defect scattering.

The presented study of the 2DELs at the bare surface of cleaved $SrTiO_3$(001) enables us to correlate the concentration of surface defects with the population of the 2DELs. Such a correlation is hard to achieve for the 2DELs confined at the interface of two materials, like the well-known interface between $LaAlO_3$ and $SrTiO_3$[14], because their atomic structure is accessible only via area- and volume-averaging techniques such are transition electron microscopy (TEM)[35] and surface X-ray diffraction (SXRD)[36], that are not particularly sensitive to the presence of (incoherently distributed) defects. It is possible that the role of Sr adatoms in inducing the downward band bending on our cleaved TiO_2 terminations is similar to the minimum number of $LaAlO_3$ layers grown on $SrTiO_3$[11] necessary to populate the interface 2DEL without the need of further excitation.

Degeneracy lifting

Correlating distinct 2DELs with their well-defined surface terminations allows us to exclude interpretations of split bands on $SrTiO_3$ surfaces as discrete 2DEL eigenstates in the surface potential wedge[4,5,37]. Our TiO_2 and SrO terminations share the same band bending according to the bottom of the heavy bands (Figs. 2e–g and 3d, e) and the Luttinger volume of the 2DEL (Supplementary Table 1), stabilized and saturated by the pinned Fermi level.

The duality of 2DELs' electronic structure in all aspects but the band splitting, calls for an explanation based on lifting of the Kramers degeneracy[7,38–40] by symmetry breaking in the lattice. The displacement of the 2DEL-hosting Ti atoms from an inversion center on the TiO_2 termination is promoted by their under-coordination at the interface with vacuum, and the out-of-plane polar distortions inherited from the strain-induced phase transition during cleaving. Such distortions are not expected to degrade the spectra quality as long as they are coherent, as observed on other metallic surfaces with sharp band splitting[41–43]. In analogy with ferroelectric systems[44–47], opposite displacements are expected on the SrO-terminated regions, but the distortions are in part suppressed by the full coordination of Ti atoms in the O-octahedra, and further rendered incoherent through the introduction of O vacancies required for band bending reversal. Furthermore, transition metal oxides are prone to self-trapping charges in the form of polarons[48–52] leading to local lattice polarization around Ti^{3+} atoms. Localized polarons can be recognized as distinct in-gap states[53–55] visible in the STS of the as-cleaved TiO_2 termination (states below the Fermi level in Fig. 3d) and in the ARPES valence band spectra of both terminations (Supplementary Note 7).

A Rashba-like lifting of the band degeneracy[56] can emerge from such coherent structural distortions on the TiO_2 termination, and has been predicted to significantly alter the spin texture due to a hybridisation between the d_{xy} and $d_{xz,yz}$ derived bands[6]. However, the Rashba effect is expected to affect the $d_{xz,yz}$ orbitals more strongly than the d_{xy} orbitals[57], because of the absence of a node along the z-direction in the latter. Furthermore, our self-energy-based analysis of the bands (Supplementary Note 11) indicates not Rashba, but Zeeman-type splitting.

In the absence of an external magnetic field, which would affect both distinct 2DELs, or an intrinsic ferromagnetic order, the Zeeman-type lifting of the 2DEL degeneracy suggests that the band splitting on the TiO_2 termination stems from magnetic interactions similar to altermagnets[40,58]. In such systems, lifting of the Kramers degeneracy arises from the in-equivalence of Ti atoms with an unpaired spin in the near surface region and does not require significant spin-orbit coupling, while certain spin configurations still generate spin textures in reciprocal space that observe time-reversal symmetry[59]. More specifically, a non-coplanar spin texture observing combined time reversal and translational symmetry ($T \cdot t$) is expected to be facilitated by slight displacements between neighbouring Ti^{3+} atoms. Along these lines, the SrO surface with a degenerate 2DEL represents an antiferromagnet with the spin sublattices connected by translation symmetry, or lacks the spin order entirely. Further experiments with spin resolution in real and reciprocal space and advanced theoretical approaches will be needed to refine this scenario.

Electron-phonon coupling

The strong coupling between electronic and structural degrees of freedom on the TiO_2-terminated surface is observed in a photoemission kink in the d_{xy}-derived bands seen in Fig. 1g and quantified previously[6] at binding energies comparable to the $SrTiO_3$ phonon bandwidth[60], hinting at sizable electron-phonon coupling (EPC)[61]. In Fig. 4a, we show the data from Fig. 1g together with the bare dispersions (parameters in Supplementary Table 1) and MDC maxima. Using our recently developed self-consistent extraction method based on Bryan's implementation of the maximum entropy method[62], we determine the Eliashberg spectral function $\alpha^2F(\omega)$[63] of the outer right-hand branch, while accounting for the photoemission matrix element[64] and quantifying the magnitudes of the electron-electron[65] and electron-impurity self-energies[66]. The real $\Sigma'(E)$ and minus imaginary $-\Sigma''(E)$ parts of the complex electron self-energy $\Sigma(E) = \Sigma'(E) + i\Sigma''(E)$[67] interpreted as being on the renormalized band[68] are shown in the inset of Fig. 4b, whereas the extracted $\alpha^2F(\omega)$ is presented in the main panel. The latter shows large spectral weight at ω=56 meV, ω=69 meV, and ω=84 meV, likely related to the respective LO_3, TO_4, and LO_4 phonon modes[60], which display moderate to strong EPC in undoped bulk $SrTiO_3$ at similar energies[69]. However, contributions from surface phonons, found in first-principles calculations at similar energies[70], cannot be excluded. Notably, due to charges accumulated at the surface in the form of the 2DEL and in-gap states, our LO_4 mode is red-shifted by approximately 8 meV with respect to first-principles calculations for undoped bulk $SrTiO_3$[69,71]. The intensity and width of the large spectral weight near ω=40 meV suggests a mixed coupling. We repeat the analysis for the outer left-hand branch (Supplementary Note 7), where the high-energy phonon modes are well-reproduced. By contrast, the mixed feature near ω=40 meV is blue-shifted for the left-hand side, suggesting that the extraction procedure is more reliable for higher phonon energies. The calculated charge density of $n_{2D} = 3.51 \times 10^{13}$ cm^{-2} for the outer

https://doi.org/10.1038/s41467-025-59258-4

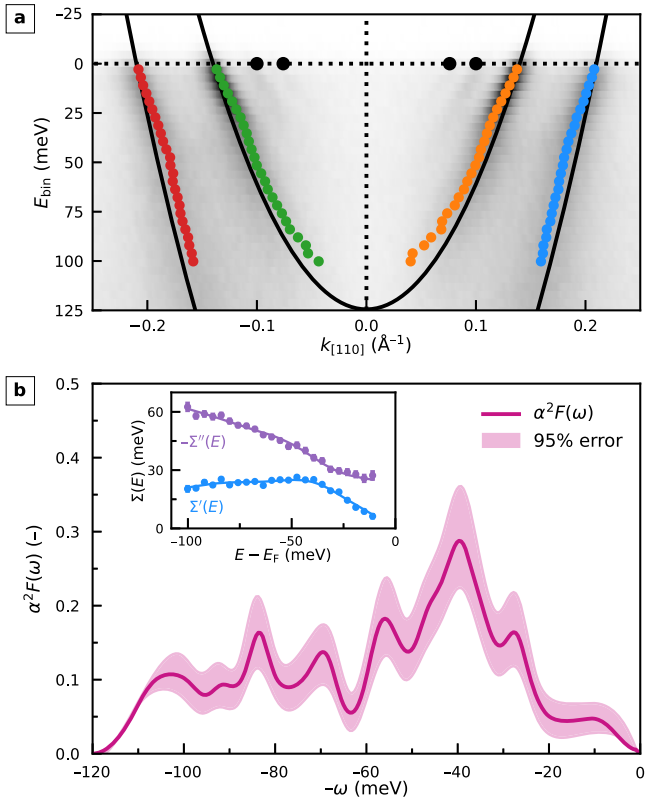

Fig. 4 | Bare bands, MDC maxima, and the right-hand outer Eliashberg spectral function for the TiO_2-terminated surface. a Bare bands (lines) and MDC maxima for the outer left (red), inner left (green), inner right (orange), and outer right (blue) branches, together with the faint band Fermi wavevectors (black dots). **b** The Eliashberg function $\alpha^2F(\omega)$ (magenta) with a 95% confidence interval (pink), determined from the right-hand outer real $\Sigma'(E)$ (blue) and minus imaginary $-\Sigma''(E)$ (purple) self-energy data shown in the inset with 95% confidence intervals and accompanied by continuous lines reconstructed from the obtained $\alpha^2F(\omega)$.

branch (Supplementary Table 1) places our results in the high-density[26] or Fermi liquid regime. Whereas the LO_4 mode was previously quantified from polaronic sidebands shifted from the band bottom by integer multiples of the mode energy[25,26], the extraction of $\alpha^2F(\omega)$ complements this approach for systems in the Fermi liquid regime. Furthermore, we quantify the electron-phonon coupling parameter $\lambda \equiv -\partial\Sigma'(E)/\partial E|_{E=E_F} = 0.63$, in reasonable agreement with λ=0.71 quantified previously[6].

The exceptional data quality for the TiO_2-terminated surface has allowed us to identify the dominant modes in the Eliashberg function and to quantify the magnitude of the EPC. The combination of spin order and the strong coupling between electronic and lattice degrees of freedom opens up the thrilling prospect of coherently controlling the spin texture, and thus also the spin-to-charge conversion[47], via ultrashort laser pulses.

In conclusion, our results highlight that a precise knowledge and control of the surface structure is crucial to understand the fundamental mechanisms and engineer the properties of 2DELs on oxide surfaces. We shine new light on 2DELs on $SrTiO_3$(001) by studying and manipulating truly bulk-terminated surfaces with unambiguous surface structure. Two well-defined terminations, differing in a single atomic layer only, host two distinct 2DELs, while the atomically ill-defined surface areas (conchoidal) can host a myriad of various 2DELs of lesser quality. The distinct 2DELs on both terminations are populated by charges from the bulk of the material, which is found to be self limiting with nearly identical band filling. Irrespective of these similarities, the Kramers degeneracy is lifted on the TiO_2, and preserved on the SrO termination, indicating a structural cause and the connection between polar distortions and non-relativistic spin order. The presence of strong electron-phonon coupling makes these surfaces a promising venue to explore such coupling mechanisms on ultrashort time scales and drive spin phenomena by external stimuli.

Methods

$SrTiO_3$single crystals with 0.5 wt% of Nb_2O_5 doping (0.7 at% Nb at the B sites of $SrBO_3$) were used in this study. The custom shaped $3.5 \times 2 \times 7$ mm^3 $SrTiO_3$ samples were purchased from MaTeck GmbH. Pristine bulk-terminated strontium titanate $SrTiO_3$(001) surfaces were achieved by cleaving $SrTiO_3$ single crystals at room temperature, through our recently developed procedures[17,22]. Cleaving devices made out of stainless steel were thoroughly cleaned ex situ before each cleaving, and were not degassed in vacuum since the investigated $SrTiO_3$(001) surfaces were not exposed to temperatures higher than room temperature. All surfaces shown in the main text were cleaved in situ: samples studied with ncAFM were cleaved inside an UHV chamber with a base pressure lower than 1×10^{-10} mbar, and samples studied with ARPES were cleaved inside a baked UHV loadlock with the pressure lower than 1×10^{-8} mbar. After cleaving, the samples were introduced to the measurement chambers with lower pressure as soon as possible, within several minutes. It is noteworthy that we do not expect significant surface chemistry to occur on our samples at room temperature where the samples were cleaved. This surface preparation technique guarantees the same surface treatment of all terminations on a single cleaved $SrTiO_3$ surface, and we did not observe temporal degradation of our samples during measurements.

ARPES measurements were performed at MAX IV synchrotron facility in Lund, Sweden, at the Bloch beamline. Cleaved samples were held at T=21.5 K during measurements in an UHV chamber with a base pressure of 1×10^{-10} mbar. All ARPES measurements were performed with linear vertical, i.e. s-polarized light and the slit of the Scienta DA30 electron analyzer was perpendicular to the scattering plane, and parallel to the [110] orientation of the crystal. All ARPES data is presented in a gray color scale, where black and white represent the maximum and the minimum photoelectron count, respectively. The experiments were reproduced on four samples during two experimental runs, with up to 100 measurement sites per sample. The separate terminations were investigated in random order, and no degradation with time was observed, i.e., spectra pertaining to a single termination did not change depending on the time between $SrTiO_3$(001) cleavage and ARPES investigation. During the ARPES measurements, ex-situ optical microscopy of the cleaved $SrTiO_3$(001) counter-piece surface was used as a guide towards well-defined areas, and the crystal edges were used as position markers to correlate ARPES, optical microscopy, and SEM. Highest-quality ARPES measurements were performed at those positions on a $SrTiO_3$(001) surface where a single domain was sufficiently large, such that we did not observe contributions from the other termination(s) when moving tens of micrometers.

Atomically resolved ncAFM measurements were performed with a low-temperature Omicron qPlus STM/AFM head, located in UHV with base pressure below 10^{-11} mbar. Bias sweeps used for recording STS measurements and Kelvin parabolas were performed in the same measurement head, by applying bias to the sample. The sample bias was modulated with a frequency of 123 Hz and an amplitude of 10 mV during STS measurements, and the current signal was differentiated using a Zürich Instruments lock-in amplifier. All STM/ncAFM measurements were performed close to the LHe temperature, i.e., at $T \approx 5$ K. Electrochemically etched tungsten tips cleaned in situ by self-sputtering with Ar^+ ions[72] were used, after thorough functionalization on a Cu(110) single crystal surface. All images in the main text were achieved by a tip that was additionally functionalized with an O atom at the tip apex[21]. Custom-design high-quality-factor (≈50000) qPlus tuning forks with a separate wire for the tunneling current were used[73].

The cantilever deflection was measured using a cryogenic differential preamplifier[74]. A bungee-cord suspension system was employed for removing mechanical noise during measurements[75].

X-ray and electron irradiation were both performed at a sample held in an electrically grounded manipulator cooled to T=100 K, in an UHV chamber with a base pressure below 1×10^{-10} mbar. The irradiated surfaces were subsequently studied after their reintroduction to the ncAFM measurement head. The samples were not warmed up following the irradiation at T=100 K as they were transferred to the measurement head using a pre-cooled wobblestick at a temperature lower than T=100 K. Al $K\alpha$ X-rays were generated from a dual-anode X-ray source (SPECS XR50, Mg/Al $K\alpha$, operated with 400 W power at a distance of ≈10 mm to the sample). Low-energy electrons were emitted from the filament of the low-energy electron diffraction (LEED) setup and were focused on the sample through integrated electron optics. Electrons with 47 eV were chosen in order to excite the Knoteck-Feibelman mechanism[31]. The spot size for X-ray irradiation was ≈1 cm^2, while the electron irradiation was focused to ≈1 mm^2. Uniform irradiation of the entire sample was achieved by rastering the sample position below a fixed X-ray or electron source. The X-ray and electron doses were varied by changing the irradiation time while all the other parameters were kept fixed. The X-ray and electron count indicated in Fig. 3 were converted from the measured sample current during irradiation, adjusted for the spot size and the duration of irradiation.

SEM images were acquired with a FEI Quanta 200F measurement setup, with a nominal vacuum of 1×10^{-5} mbar. The working distance was ≈8 mm. Secondary electrons were detected with an Everhart-Thornley detector. All SEM images are presented in a gray color scale, where white and black represent the maximum and the minimum secondary electron count, respectively. All surfaces imaged with SEM were acquired under same conditions. An electron energy of 5 kV was used. SEM imaging was performed at the USTEM facility of the TU Wien.

Optical photographs were taken using an Olympus SZX12 microscope equipped with a DF PLAPO 1X PF lens, and an attached Olympus E-330 camera with a 14–45 mm lens.

Data acquired with ncAFM was processed for drift correction, background subtraction, and noise reduction using ImageJ software (imagej.net) augmented with procedures developed by Michael Schmid. ARPES data was analyzed and processed using the pesto Python library (pesto.readthedocs.io) developed by Craig Polley, in combination with IGOR Pro software (wavemetrics.com). Self-energy and Eliashberg function extraction were performed with a private version of xARPES, whose description is laid out in Supplementary Notes 8–11.

Data availability

The data that support the analysis for this study are available from the corresponding authors upon request.

Code availability

An initial version of the xARPES code, which contains some of the features used in this work, is available at https://xarpes.github.io/, whereas the remainder of the features used here are scheduled for a future release.

References

1. Müller, K. A. & Burkard, H. $SrTiO_3$: An intrinsic quantum paraelectric below 4 K. *Phys. Rev. B* **19**, 3593 (1979).
2. Yang, Z. et al. Epitaxial $SrTiO_3$ films with dielectric constants exceeding 25,000. *Proc. Natl. Acad. Sci. USA* **119**, e2202189119 (2022).
3. Santander-Syro, A. F. et al. Two-dimensional electron gas with universal subbands at the surface of $SrTiO_3$. *Nature* **469**, 189 (2011).
4. Meevasana, W. et al. Creation and control of a two-dimensional electron liquid at the bare $SrTiO_3$ surface. *Nat. Mater.* **10**, 114 (2011).
5. Wang, Z. et al. Anisotropic two-dimensional electron gas at $SrTiO_3$(110). *Proc. Natl. Acad. Sci. USA* **111**, 3933–3937 (2014).
6. King, P. D. C. et al. Quasiparticle dynamics and spin–orbital texture of the $SrTiO_3$ two-dimensional electron gas. *Nat. Commun.* **5**, 3414 (2014).
7. Guedes, E. B. et al. Single spin-polarized fermi surface in $SrTiO_3$ thin films. *Phys. Rev. Res.* **2**, 033173 (2020).
8. Guedes, E. B. et al. Universal structural influence on the 2D electron gas at $SrTiO_3$ surfaces. *Adv. Sci.* **8**, 2100602 (2021).
9. Rebec, S. N. et al. Dichotomy of the photo-induced 2-dimensional electron gas on $SrTiO_3$ surface terminations. *Proc. Natl. Acad. Sci. USA* **116**, 16687–16691 (2019).
10. Yan, X. et al. Origin of the 2D electron gas at the $SrTiO_3$ surface. *Adv. Mater.* **34**, 2200866 (2022).
11. Thiel, S., Hammerl, G., Schmehl, A., Schneider, C. W. & Mannhart, J. Tunable quasi-two-dimensional electron gases in oxide heterostructures. *Science* **313**, 1942–1945 (2006).
12. Okamoto, S., Millis, A. J. & Spaldin, N. A. Lattice relaxation in oxide heterostructures: $LaTiO_3/SrTiO_3$ superlattices. *Phys. Rev. Lett.* **97**, 056802 (2006).
13. Chikina, A. et al. Orbital ordering of the mobile and localized electrons at oxygen-deficient $LaAlO_3/SrTiO_3$ interfaces. *ACS Nano* **12**, 7927–7935 (2018).
14. Ohtomo, A. & Hwang, H. Y. A high-mobility electron gas at the $LaAlO_3/SrTiO_3$ heterointerface. *Nature* **427**, 423 (2004).
15. Seo, J. et al. Feld-induced modulation of two-dimensional electron gas at $LaAlO_3/SrTiO_3$ interface by polar distortion of $LaAlO_3$. *Nat. Communs.* **15**, 5268 (2024).
16. Takagi, H. & Hwang, H. Y. An emergent change of phase for electronics. *Science* **327**, 1601–1602 (2010).
17. Sokolović, I., Schmid, M., Diebold, U. & Setvín, M. Incipient ferroelectricity: A route towards bulk-terminated $SrTiO_3$. *Phys. Rev. Mater.* **3**, 034407 (2019).
18. Sokolović, I. et al. Quest for a pristine unreconstructed $SrTiO_3$(001) surface: An atomically resolved study via noncontact atomic force microscopy. *Phys. Rev. B* **103**, L241406 (2021).
19. Noguera, C. Polar oxide surfaces. *J. Phys. Condens. Matter* **12**, R367 (2000).
20. Goniakowski, J., Finocchi, F. & Noguera, C. Polarity of oxide surfaces and nanostructures. *Rep. Prog. Phys.* **71**, 016501 (2007).
21. Sokolović, I. et al. Resolving the adsorption of molecular O_2 on the rutile TiO_2(110) surface by noncontact atomic force microscopy. *Proc. Natl. Acad. Sci. USA* **117**, 14827–14837 (2020).
22. Sokolović, I., Schmid, M., Diebold, U. & Setvín, M. How to cleave cubic perovskite oxides. *Rev. Sci. Instr.* **96**, 035113 (2025).
23. Kato, T. et al. Polarity-dependent charge density wave in the kagome superconductor CsV_3Sb_5. *Phys. Rev. B* **106**, L121112 (2022).
24. To, D. Q. et al. Spin to charge conversion at Rashba-split $SrTiO_3$ interfaces from resonant tunneling. *Phys. Rev. Res.* **3**, 043170 (2021).
25. Chen, C., Avila, J., Frantzeskakis, E., Levy, A. & Asensio, M. C. Observation of a two-dimensional liquid of fröhlich polarons at the bare $SrTiO_3$ surface. *Nature Commun.* **6**, 8585 (2015).
26. Wang, Z. et al. Tailoring the nature and strength of electron–phonon interactions in the $SrTiO_3$(001) 2D electron liquid. *Nat. Mater.* **15**, 835 (2016).
27. Plumb, N. C. et al. Mixed dimensionality of confined conducting electrons in the surface region of $SrTiO_3$. *Phys. Rev. Lett.* **113**, 086801 (2014).
28. Chikina, A. et al. X-ray writing of metallic conductivity and oxygen vacancies at silicon/$SrTiO_3$ interfaces. *Adv. Func. Mater.* **29**, 1900645 (2019).
29. McKeown Walker, S. et al. A laser-ARPES view of the 2D electron systems at $LaAlO_3/SrTiO_3$ and Al/$SrTiO_3$ interfaces. *Adv. Electron. Mater.* **8**, 2101376 (2022).

30. Alonso, M., Cimino, R. & Horn, K. Surface photovoltage effects in photoemission from metal-GaP(110) interfaces: Importance for band bending evaluation. *Phys. Rev. Lett.* **64**, 1947 (1990).
31. Knotek, M. L. & Feibelman, P. J. Ion desorption by core-hole Auger decay. *Phys. Rev. Lett.* **40**, 964 (1978).
32. Dulub, O. et al. Electron-induced oxygen desorption from the TiO_2(011)-2×1 surface leads to self-organized vacancies. *Science* **317**, 1052–1056 (2007).
33. Setvín, M. et al. Polarity compensation mechanisms on the perovskite surface $KTaO_3$(001). *Science* **359**, 572–575 (2018).
34. Queiroz, R. et al. Sputtering-induced reemergence of the topological surface state in Bi_2Se_3. *Phys. Rev. B* **93**, 165409 (2016).
35. Song, K. et al. Electronic and structural transitions of $LaAlO_3/SrTiO_3$ heterostructure driven by polar field-assisted oxygen vacancy formation at the surface. *Adv. Sci.* **8**, 2002073 (2021).
36. Salluzzo, M. et al. Structural and electronic reconstructions at the $LaAlO_3/SrTiO_3$ interface. *Adv. Mater.* **25**, 2333 (2013).
37. Bahramy, M. S. et al. Emergent quantum confinement at topological insulator surfaces. *Nat. Commun.* **3**, 1159 (2012).
38. Kramers, H. A. Théorie générale de la rotation paramagnétique dans les cristaux. *Proc. Acad. Amst.* **33**, 959 (1930).
39. Santander-Syro, A. F. et al. Giant spin splitting of the two-dimensional electron gas at the surface of $SrTiO_3$. *Nat. Mat.* **13**, 1085–1090 (2014).
40. Krempaský, J. et al. Altermagnetic lifting of Kramers spin degeneracy. *Nature* **626**, 517–522 (2024).
41. Ast, C. R. et al. Giant spin splitting through surface alloying. *Phys. Rev. Lett.* **98**, 186807 (2007).
42. Hsieh, D. et al. Observation of unconventional quantum spin textures in topological insulators. *Science* **323**, 919 (2009).
43. Krempaský, J. et al. Fully spin-polarized bulk states in ferroelectric GeTe. *Phys. Rev. Res.* **2**, 013107 (2020).
44. Krempaský, J. et al. Operando imaging of all-electric spin texture manipulation in ferroelectric and multiferroic Rashba semiconductors. *Phys. Rev. X* **8**, 021067 (2018).
45. Rinaldi, C. et al. Ferroelectric control of the spin texture in GeTe. *Nano Lett.* **18**, 2751 (2018).
46. Djani, H. et al. Rationalizing and engineering Rashba spin-splitting in ferroelectric oxides. *npj Quantum Mater.* **4**, 1–6 (2019).
47. Noël, P. et al. Non-volatile electric control of spin–charge conversion in a $SrTiO_3$ Rashba system. *Nature* **580**, 483–486 (2020).
48. Franchini, C., Reticcioli, M., Setvin, M. & Diebold, U. Polarons in materials. *Nat. Rev. Mater.* **6**, 560 (2021).
49. Reticcioli, M. et al. Interplay between adsorbates and polarons: CO on rutile TiO_2(110). *Phys. Rev. Lett.* **122**, 016805 (2019).
50. Yim, C. M. et al. Engineering polarons at a metal oxide surface. *Phys. Rev. Lett.* **117**, 116402 (2016).
51. Kaviani, M., Strand, J., Afanas'ev, V. V. & Shluger, A. L. Deep electron and hole polarons and bipolarons in amorphous oxide. *Phys. Rev. B* **94**, 020103 (2016).
52. Di Valentin, C. & Selloni, A. Bulk and surface polarons in photoexcited anatase TiO_2. *J. Phys. Chem. Lett.* **2**, 2223 (2011).
53. Wang, Z. et al. Surface chemistry on a polarizable surface: Coupling of CO with $KTaO_3$(001). *Sci. Adv.* **8**, eabq1433 (2022).
54. Reticcioli, M. et al. Competing electronic states emerging on polar surfaces. *Nat. Commun.* **13**, 1 (2022).
55. Ellinger, F., Shafiq, M., Ahmad, I., Reticcioli, M. & Franchini, C. Small polaron formation on the Nb-doped $SrTiO_3$(001) surface. *Phys. Rev. Mater.* **7**, 064602 (2023).
56. Rashba, E. Properties of semiconductors with an extremum loop. I. Cyclotron and combinational resonance in a magnetic field perpendicular to the plane of the loop. *Sov. phys., Solid state* **2**, 1109 (1960).
57. Varotto, S. et al. Direct visualization of Rashba-split bands and spin/orbital-charge interconversion at $KTaO_3$ interfaces. *Nat. Commun.* **13**, 6165 (2022).
58. Šmejkal, L., Sinova, J. & Jungwirth, T. Emerging research landscape of altermagnetism. *Phys. Rev. X* **12**, 040501 (2022).
59. Hellenes, A. B., Jungwirth, T., Sinova, J. & Šmejkal, L. Exchange spin-orbit coupling and unconventional p-wave magnetism. *arXiv preprint arXiv:2309.01607* (2023).
60. Vogt, H. Hyper-Raman tensors of the zone-center optical phonons in $SrTiO_3$ and $KTaO_3$. *Phys. Rev. B* **38**, 5699–5708 (1988).
61. Johnson, P. D. et al. Doping and temperature tependence of the mass enhancement observed in the cuprate $Bi_2Sr_2CaCu_2O_{8+\delta}$. *Phys. Rev. Lett.* **87**, 177007 (2001).
62. Bryan, R. K. Maximum entropy analysis of oversampled data problems. *Eur. Biophys. J.* **18**, 165–174 (1990).
63. Grimvall, G.*The Electron–Phonon Interaction in Metals* (North-Holland, Amsterdam, 1981).
64. Moser, S. An experimentalist's guide to the matrix element in angle resolved photoemission. *J. Electron Spectrosc. Relat. Phenom.* **214**, 29–52 (2017).
65. Jungwirth, T. & MacDonald, A. H. Electron-electron interactions and two-dimensional–two-dimensional tunneling. *Phys. Rev. B* **53**, 7403–7412 (1996).
66. Jiang, J. et al. High-Resolution Angle-Resolved Photoemission Study of the Al(100) Single Crystal. *e-J. Surf. Sci. Nanotechnol.* **7**, 57–60 (2009).
67. Damascelli, A. Probing the electronic structure of complex systems by ARPES. *Phys. Scr.* **T109**, 61 (2004).
68. Verga, S., Knigavko, A. & Marsiglio, F. Inversion of angle-resolved photoemission measurements in high-T_c cuprates. *Phys. Rev. B* **67**, 054503 (2003).
69. Zhou, J.-J., Hellman, O. & Bernardi, M. Electron-Phonon Scattering in the Presence of Soft Modes and Electron Mobility in $SrTiO_3$ Perovskite from First Principles. *Phys. Rev. Lett.* **121**, 226603 (2018).
70. Xie, Y. et al. Oxygen Vacancy Induced Flat Phonon Mode at FeSe /$SrTiO_3$ interface. *Sci Rep* **5**, 10011 (2015).
71. Cancellieri, C. et al. Polaronic metal state at the $LaAlO_3/SrTiO_3$ interface. *Nat. Commun.* **7**, 10386 (2016).
72. Setvín, M. et al. Ultrasharp tungsten tips—characterization and nondestructive cleaning. *Ultramicroscopy* **113**, 152–157 (2012).
73. Giessibl, F. J. Sensor for noncontact profiling of a surface. US patent 8,393,009 (2013).
74. Huber, F. & Giessibl, F. J. Low noise current preamplifier for qPlus sensor deflection signal detection in atomic force microscopy at room and low temperatures. *Rev. Sci. Instrum.* **88**, 073702 (2017).
75. Schmid, M., Setvín, M. & Diebold, U. Device for suspending a load in a vibration-insulated manner. US patent WO/2018/037102 (2018).

Acknowledgements

I.S., M.Sc., U.D. and M.Se. acknowledge support by the Austrian Science Fund (FWF) projects Solids4Fun (F-1243) and SuPer (P32148-N36). U.D. also acknowledges support by the FWF SFB project TACO (Grant-DOI:10.55776/F81); for open access purposes the author has applied a CC BY public copyright license to any author accepted manuscript version arising from this submission. T.P. v.W. is a Research Fellow of the F.R.S.-FNRS. S.P. acknowledges financial support from the F.R.S.-FNRS (Belgium) and the Walloon Region in the strategic axe FRFS-WEL-T. M.R. and E.B.G were supported by SNSF Research Grant 200021_182695. M.Se. also acknowledges support from the Czech Science Foundation GACR 20-21727X and GAUK Primus/20/SCI/009. F.G. and J.H.D. acknowledge support from the Swiss National Science Foundation (SNSF) Project No. 200021-200362. We acknowledge MAX IV Laboratory for time on the Bloch Beamline under Proposal 20210244. Research conducted at MAX IV, a Swedish national user facility, is supported by the Swedish Research council under contract 2018-07152, the Swedish Governmental Agency for Innovation Systems under contract 2018-04969, and Formas under contract 2019-02496.

Author contributions

I.S., E.B.G., F.G., C.P. and J.H.D. acquired, analyzed, and presented experimental ARPES data; I.S. acquired, analyzed, and presented experimental ncAFM/STM data; T.P.v.W., S.P. and J.H.D. analyzed experimental ARPES data to extract 2DEL parameters and extracted self-energies and the Eliashberg function; S.P., M.Sc., U.D., M.R., M.Se. and J.H.D. verified the presented findings; U.D., M.Se. and J.H.D. conceived the project and acquired funding. I.S., E.B.G., T.P.v.W. and J.H.D. compiled the first paper draft, all Authors wrote and proofed the final version of the manuscript.

Competing interests

The authors declare no competing interests.

Additional information

Supplementary information The online version contains supplementary material available at https://doi.org/10.1038/s41467-025-59258-4.

Correspondence and requests for materials should be addressed to Igor Sokolović or J. Hugo Dil.

Peer review information *Nature Communications* thanks Rui-Hua He and the other, anonymous, reviewer(s) for their contribution to the peer review of this work. A peer review file is available.